

# (INVITED)Adjustable near-infrared fluorescence lifetime emission of biocompatible rare-earth-doped nanoparticles for *in vivo* multiplexing

Jingke Yao<sup>a</sup>, Gabriel López-Peña<sup>b</sup>, José Lifante<sup>c</sup>, M. Carmen Iglesias-de la Cruz<sup>c,d</sup>,  
Riccardo Marin<sup>a</sup>, Emma Martín Rodríguez<sup>b,d</sup>, Daniel Jaque<sup>a,d</sup>, Dirk H. Ortgies<sup>a,d,\*</sup>

<sup>a</sup> Nanomaterials for BioImaging Group, Departamento de Física de Materiales, Universidad Autónoma de Madrid, C/ Francisco Tomás y Valiente 7, 28049, Madrid, Spain

<sup>b</sup> Nanomaterials for BioImaging Group, Departamento de Física Aplicada, Universidad Autónoma de Madrid, C/ Francisco Tomás y Valiente 7, 28049, Madrid, Spain

<sup>c</sup> Nanomaterials for BioImaging Group, Departamento de Fisiología, Universidad Autónoma de Madrid, C/ Arzobispo Morcillo s/n, 28029, Madrid, Spain

<sup>d</sup> Nanomaterials for BioImaging Group, Instituto Ramón y Cajal de Investigación Sanitaria IRYCIS, Ctra de Colmenar km 9,300, 28034, Madrid, Spain

## ARTICLE INFO

### Keywords:

Rare-earth-doped nanoparticles  
Bioimaging  
Infrared imaging  
Multiplexing  
Fluorescence lifetime

## ABSTRACT

Rare-earth-doped inorganic nanocrystals are an important class of nanoparticles for bioimaging applications due to the facility of providing them with tailored emissions in the visible and near-infrared regions of the electromagnetic spectrum. Recently it has become of interest to engineer the dopant composition of these materials in order to enable multiplexed lifetime imaging for autofluorescence-free *in vivo* bioimaging. Herein we report a simple approach to obtain different fluorescence lifetimes for the Yb<sup>3+</sup> emission (<sup>2</sup>F<sub>5/2</sub> → <sup>2</sup>F<sub>7/2</sub>) in Nd<sup>3+</sup>, Yb<sup>3+</sup>, Tm<sup>3+</sup> co-doped NaGdF<sub>4</sub> nanoparticles by only changing their crystal size while keeping their hydrodynamic diameter constant. This allowed straightforward transformation of infrared images in the time domain into lifetime maps. The particles were then deployed as *in vivo* contrast agents for near-infrared imaging in a mouse demonstrating their multiplexing capability.

## 1. Introduction

Ever increasing needs for modern diagnostic approaches have driven the development of optical imaging techniques in recent years [1,2]. They promise some advantages over state-of-the-art technologies like magnetic resonance imaging or radio-isotope-based approaches, i.e., mainly speed of imaging, reduced costs due to the employment of common optical elements, and the use of non-ionizing radiation [3,4]. Infrared fluorescence imaging has garnered special interest because biological tissues are partially transparent in the near-infrared (NIR) region of the electromagnetic spectrum [5,6]. Specifically, working in the NIR transparency windows (NIR-I: 680–950 nm, NIR-IIa: 1000–1350 nm, NIR-IIb: 1500–1700 nm) [7,8] the largest penetration depth in biological tissues is obtained because tissue absorbance and scattering are reduced. Hence *in vivo* NIR fluorescence imaging has become possible at the subcutaneous level or even as whole-body imaging technique in small animal models [9–11].

This development has gone hand in hand with the investigation of new materials as contrast agents for NIR imaging. Carbon-based

nanotubes and dots [12–15], semiconducting organic polymers and nanoparticles (NPs) [16–19], quantum dots [20–22], Ag<sub>2</sub>S nanodots [23–25], NIR-II dyes [26–30], and rare-earth-doped nanoparticles (RENPs) [31–34] have all been proposed for this application. These studies showed that *in vivo* autofluorescence presents a hindrance when working at wavelengths up to 1200 nm [35,36]. Therefore, techniques to bypass endogenous autofluorescence have become of particular interest as of late [37–39], among which time-gated imaging – based on NPs with long fluorescence lifetimes – has increased in relevancy [40–42]. This approach takes advantage of the fact that endogenous fluorophores of biological tissues have fluorescence lifetimes in the nanosecond range, while contrast agents can be engineered to present lifetimes from several microseconds to milliseconds [43–48]. This is especially true in the case of RENPs, whose lanthanide dopants' f-f transitions are a showcase for long lifetimes with sharp emission peaks [49–53].

Lifetime-based *in vivo* imaging is not only advantageous for autofluorescence-free imaging, but it also opens the possibility of *in vivo* multiplexed imaging. Multiplexing refers here to the capability to

\* Corresponding author. Nanomaterials for BioImaging Group, Departamento de Física de Materiales, Universidad Autónoma de Madrid, C/ Francisco Tomás y Valiente 7, 28049, Madrid, Spain.

E-mail address: [dirk.ortgies@uam.es](mailto:dirk.ortgies@uam.es) (D.H. Ortgies).

<https://doi.org/10.1016/j.omx.2022.100225>

Received 22 October 2022; Received in revised form 7 December 2022; Accepted 15 December 2022

Available online 23 December 2022

2590-1478/© 2023 The Authors. Published by Elsevier B.V. This is an open access article under the CC BY license (<http://creativecommons.org/licenses/by/4.0/>).

distinguish different contrast agents in *in vivo* fluorescence images. When it is performed in the visible range, it is typically based on different colours (spectral multiplexing) [54–58]. Differences in fluorescence lifetimes enable multiplexing in the time domain, which presents a series of advantages especially for NIR-II *in vivo* imaging. These advantages are: the ease of signal separation by time-gating with standard InGaAs infrared cameras, the use of cost-effective illumination sources – like diodes that are easily modulated with rise times of few microseconds –, and the reliance on the same spectral emission, which therefore presents the exact same tissue-photon interaction only minimally affecting its intensity [59]. In contrast, most available infrared contrast agents work in the same spectral range or show great overlap and could only be differentiated with expensive hyperspectral imaging technology and unmixing algorithms [60]. Therefore over the last years the combination of time-domain multiplexing and time-gating in the NIR started to be developed [61], and RENPs for multiplexing were synthesized via different approaches. Among these approaches are the variation of dopant concentrations [41,62], growth of intermediate shells of different thicknesses to delay the energy transfer, combinations of shells and concentration changes [63,64], and mixed approaches [65–67].

For RENPs, we recently demonstrated the superior performance of  $\text{Nd}^{3+}$ ,  $\text{Yb}^{3+}$ ,  $\text{Tm}^{3+}$  co-doped  $\text{NaGdF}_4$  NPs in time-gated imaging in the NIR [41]. Their dopant combination enabled a long emission lifetime due to various energy transfers between the lanthanide ions, resulting in a dominance of the  $\text{Yb}^{3+} {}^2\text{F}_{5/2}$  state [68]. Excitation at 800 nm sensitizes the  $\text{Nd}^{3+}$  dopant ( ${}^4\text{I}_{9/2} \rightarrow {}^4\text{F}_{5/2}$ ) but also directly  $\text{Tm}^{3+}$  ( ${}^3\text{H}_6 \rightarrow {}^3\text{H}_4$ ), which is followed by energy transfer from  $\text{Nd}^{3+}$  to  $\text{Yb}^{3+}$  ( ${}^4\text{F}_{3/2} \rightarrow {}^2\text{F}_{5/2}$ ). This enables the  $\text{Yb}^{3+}$  emission ( ${}^2\text{F}_{5/2} \rightarrow {}^2\text{F}_{7/2}$ ) but also results in energy transfer upconversion to  $\text{Tm}^{3+}$  allowing it to reach the  ${}^1\text{I}_6$  level. At this point  $\text{Gd}^{3+}$  in the crystal matrix is not inert anymore but can accept the energy in another energy transfer ( ${}^1\text{I}_6 \rightarrow {}^6\text{P}_{7/2}$ ) and transfer it back to an excited  $\text{Nd}^{3+}$  state ( ${}^6\text{P}_{7/2} \rightarrow {}^2\text{P}_{1/2}$ ), from which it moves on to re-excite  $\text{Yb}^{3+}$  to the  ${}^2\text{F}_{5/2}$  state. As a consequence longer than usual lifetimes for  $\text{Yb}^{3+}$  are achieved (see Fig. S1 in the Supplementary Data). Despite the good results obtained so far, the use of  $\text{Nd}^{3+}$ ,  $\text{Yb}^{3+}$ ,  $\text{Tm}^{3+}$  co-doped  $\text{NaGdF}_4$  nanoparticles (from now on  $\tau\text{NPs}$ ) for multiplexed *in vivo* imaging has not yet been demonstrated. For that, the development of a strategy to modify their lifetime in a controlled manner is required.

Herein we present biocompatible  $\tau\text{NPs}$  with the same effective hydrodynamic radius but different nanocrystal size that behave as promising contrast agents for lifetime-based multiplexed *in vivo* imaging. These nanoparticles are expected to display the same biological behaviour – since one decisive factor for biodistribution is the hydrodynamic size – [69,70] but different spectroscopic properties (e.g., lifetimes), making, for instance, advanced and detailed imaging of different cells and tissues within the same organ possible. Multiplexed images of  $\tau\text{NPs}$  with the same hydrodynamic radius in the same individual generate also the possibility of single-shot pharmacodynamic studies on the impact of administration routes in the distribution dynamics of identical nanoparticles. The potential of these contrast agents for lifetime-based multiplexed imaging is herein demonstrated by the design and development of simple imaging experiments at the *in vivo* level.

## 2. Experimental section

The synthesis of the polyacrylic acid (PAA) coated  $\text{NaGdF}_4$ : 3%  $\text{Nd}^{3+}$ , 2%  $\text{Yb}^{3+}$ , 0.2%  $\text{Tm}^{3+}$  NPs and their characterization experiments are described in detail in the Supplementary Data. Of special importance are the following procedures.

### 2.1. Fluorescence imaging

Fluorescence images were obtained employing a Photon SWIR *in vivo* imaging system developed in the Horizon 2020 NanoTBTech project by

Biospace Lab (Nesles-la-Vallée, France). The system contains an InGaAs CCD camera working in the 1000–1700 nm spectral range (WiDi SenS 640V-ST, New Imaging Technologies, France) with a long pass filter at 1000 nm (Thorlabs FEL1000) placed in front. A fiber-coupled 808 nm laser diode (LIMO) with a maximum output power of 6 W is also part of the system and its beam is passed through a variable lens for illumination of the samples/animal with a max (peak) power density of 0.5 W/cm<sup>2</sup> and an average power density of 17 mW/cm<sup>2</sup>. The system is configured to provide 10 ms pulses (resulting energy is 0.06 J) with a pulse-to-pulse separation of 35 ms (pulse repetition rate 28 Hz) and an initial time delay between the end of the laser pulse and camera acquisition of 20  $\mu\text{s}$ . This initial delay is increased by 20  $\mu\text{s}$  between each picture (exposure time 20 ms) and a series of 500 pictures was obtained, resulting in a final delay of 10 ms.

### 2.2. Time domain analysis of fluorescence images

To obtain fluorescence lifetime images, a series of time-gated fluorescence intensity images were acquired, each one at a different time delay after excitation. The intensity decay of each pixel in the image was afterwards analysed to obtain a value related to the fluorescence lifetime. Complex intensity decays usually require complex models to obtain the lifetime value [71,72], however, in the case of a single exponential of the form:

$$I = I_0 \exp(-t / \tau) \quad (\text{Equation 1})$$

the lifetime can be easily obtained after normalization by direct integration of the intensity decay profile:

$$\int_0^\infty I dt = \int_0^\infty I_0 \exp(-t / \tau) dt = I_0 \tau \quad (\text{Equation 2})$$

where  $I$  refers to the intensity for a given time moment ( $t$ ),  $I_0$  to the initial intensity ( $I_0 = 1$  due to normalization), and  $\tau$  to the fluorescence lifetime. In the case of a multi-exponential decay process, this approach can still be used to obtain a parameter that can be defined as “combined lifetime” ( $\tau_c$ ), which is the multiplicative inverse of the lifetimes of each process:

$$\tau_c = \frac{\prod_{i=1}^N \tau_i}{\sum_{i=1}^N \tau_i} \quad (\text{Equation 3})$$

The value of the integral of the set of data was estimated from the time evolution of the intensity of each pixel by using the trapezoid rule, i.e., by approximating the curve as a series of trapezoids and calculating its area. The combined lifetime was then approximated as:

$$\tau_c \approx \frac{\int_0^{t_f} I dt}{I_0} \approx \frac{1}{2I_0} \sum_{n=1}^N (t_{n+1} - t_n) [I(t_{n+1}) + I(t_n)] \quad (\text{Equation 4})$$

This method provides a good approximation to the lifetime if the sampling time ( $t_f$ ) is long enough to ensure that the intensity of the fluorophore has decayed to the background level and has a low computational cost compared to methods based on the fitting of the intensity decay curve to exponential models.

### 2.3. Animal experiments

All procedures involving animal experiments were approved by the regional authority for animal experimentation of the Comunidad de Madrid and were conducted in agreement with the Universidad Autónoma de Madrid Ethics Committee and in compliance with the European Union directives 63/2010UE and Spanish regulation RD 53/2013. One CD1 female mouse (weight, 30 g; age, 8 weeks old) was employed for the *in vivo* experiment under isoflurane anesthesia (4%

isoflurane 2 L/min O<sub>2</sub> for induction, 1.5% isoflurane 0.5 L/min O<sub>2</sub>, for maintenance).  $\tau$ NPs were administered subcutaneously by injection into the left (50  $\mu$ L 20 nm  $\tau$ TPs, 5 mg/mL in sterile Phosphate Buffered Saline –PBS–) and right dorsal flank (50  $\mu$ L 35 nm  $\tau$ NPs, 1 mg/mL in sterile PBS) of the animal with a 30-gauge sterile needle. The injection depth was estimated to be around 1 mm. After the imaging experiments were complete, euthanasia was performed beheading the animal under 5% of isoflurane inhaled anesthesia, 2 L/min O<sub>2</sub>. In order to ascertain the possible clearing of the subcutaneous injection through the bloodstream towards different tissues, the organs were dissected immediately after the sacrifice of the animal and illuminated in a control experiment under time-gating conditions, but no signal was observed (see the Supplementary Data).

### 3. Results and discussion

Nd<sup>3+</sup>, Tm<sup>3+</sup>, Yb<sup>3+</sup> co-doped NPs were synthesized modifying previously reported syntheses with a layer-by-layer method in order to achieve NaGdF<sub>4</sub>: 3% Nd<sup>3+</sup>, 2% Yb<sup>3+</sup>, 0.2% Tm<sup>3+</sup> ( $\tau$ NPs) of five different sizes [41,73]. Fig. 1 shows transmission electron microscopy (TEM) images of 9 nm (A), 15 nm (B), 20 nm (C), 35 nm (D), and 42 nm (E)  $\tau$ NPs that all demonstrate narrow size-distributions further illustrated in Fig. 1F and hexagonal shapes, indicating crystallization in the beta-phase. This was confirmed by powder x-ray diffraction (XRD) as illustrated in Fig. 1G, which also shows an expected narrowing of the reflections with increasing crystal size. Lastly, the  $\tau$ NPs were transferred into aqueous dispersion via ligand exchange with polyacrylic acid (PAA) as described in detail in the Supplementary Data (see also the Fourier-transform infrared spectra in Fig. S2). The PAA coating provides excellent aqueous dispersibility and biocompatibility to the  $\tau$ NPs [74, 75]. Moreover, as a consequence of the swelling of the polymer, five aqueous dispersions (1 mg/mL) of  $\tau$ NPs with similar hydrodynamic radii (Fig. 1H) and  $\zeta$ -potential (see Fig. S3) were obtained. The comparability and validity of these radii is confirmed through clear shapes and similarities of the correlation curves of the DLS measurements (see Fig. S4). Therefore, our  $\tau$ NPs feature analogous surface chemistry, expected biological interactions, and effective size, while being based on different core sizes responsible for their size-dependent luminescence properties.

Fig. 2 summarizes the NIR emission properties of the  $\tau$ NPs and their potential for multiplexing. Fig. 2A shows that increasing the core-size from 9 to 42 nm results in improved emission intensity in all three observed transitions, at 980 nm (Yb<sup>3+</sup>: <sup>2</sup>F<sub>5/2</sub> → <sup>2</sup>F<sub>7/2</sub>), 1060 nm (Nd<sup>3+</sup>: <sup>4</sup>F<sub>3/2</sub> → <sup>4</sup>F<sub>11/2</sub>) and 1300 nm (Nd<sup>3+</sup>: <sup>2</sup>F<sub>3/2</sub> → <sup>2</sup>F<sub>13/2</sub>). This trend is reflected in the fluorescence lifetimes of Yb<sup>3+</sup> (Fig. 2B) measured at 980 nm showing a great variation from 760  $\mu$ s at 9 nm to 1510  $\mu$ s at 42 nm (the emission lifetimes in hexane can be found in Fig. S5 for comparison), basically doubling the lifetime of the  $\tau$ NPs. These different

lifetimes lay the foundation for multiplexing in the time domain. Their trend follows the surface-to-volume ratio due to the decreasing surface quenching with reduced surface area relative to volume [76–79]. This is highlighted in Fig. 2C, where the increasing lifetime with size is shown together with the inverse trend when illustrating the relationship with the surface-to-volume-ratio. This demonstrates that at larger sizes - when the surface of the  $\tau$ NPs is not dominant anymore - the increase in lifetime comes to a stand and the fluorescence lifetime corresponding to the bulk material is observed due to the now proportionally negligible influence of quenching events at the surface states [41,68]. Note that this was expected because as the surface-to-volume ratio decreases the contribution of non-radiative events such as transfer to surface states, a consequence of surface defects, and solvent molecules is also reduced. Under these conditions, radiative de-excitations taking place in the volume (far from the surface) become dominant. Therefore, this lifetime series underscores how it is possible to readily tune the optical properties of RENPs with this elemental composition by merely changing their size, thus making them apt for multiplexing in the time domain.

As described in the Experimental Section, our approach to lifetime imaging is based on the integration of the decay curves of each pixel for the formation of the image in the time domain. This is a faster yet precise approach possible with the  $\tau$ NPs as can be seen from the Supplementary Data's Fig. S6, which shows the comparison with the computationally more intensive fitting of a stretched exponential function to every pixel. Only for the shortest lifetimes a minimal difference can be observed but this does not affect the multiplexed imaging.

In order to test these NPs for their employability as *in vivo* contrast agents, we investigated their capability in time-gated imaging with animal tissues as illustrated in Fig. 3. The three dispersions with large differences in lifetimes were placed in the time-gated imaging system and a series of infrared images with increasing delays were taken and used to build up a lifetime map. Fig. 3A shows the optical image of the three dispersions, Fig. 3B the infrared image and Fig. 3C the merged picture. Finally, Fig. 3D shows the lifetime map that was obtained by analysing the time-gated images and integrating each pixel decay over the series to determine their lifetime. A clear differentiation of the three different dispersions is possible, making them valuable contrast agents for multiplexing. Fig. 3E–H and I–L show the repetition of these experiments with a layer of biological tissue placed on top (2 and 5 mm of chicken breast, respectively). The presence of this tissue results in a loss of NIR intensity and an increase in scattering as can be observed from the infrared image and is also visible in the lifetime map. Nevertheless, the different lifetimes can still be clearly visualized, demonstrating the advantage of working at the same wavelength in the NIR-II, where tissue-induced extinction is minimized.

It should be noted at this point, that the three samples here analysed, although providing similar emission intensities, show clearly different

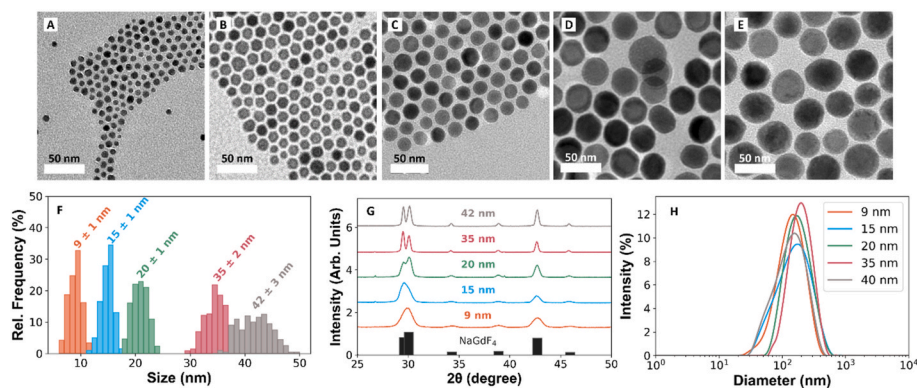


**Fig. 1.** Morphological characterization. TEM images (A, B, C, D and E) and size distributions (F) of five different sizes of NaGdF<sub>4</sub>: 3% Nd<sup>3+</sup>, 2% Yb<sup>3+</sup>, 0.2% Tm<sup>3+</sup> RENPs. Scale bar: 50 nm. (G) XRD pattern of the RENPs. (H) Dynamic light scattering (DLS) measurements performed on five different sizes of  $\tau$ NPs modified with PAA and dispersed in PBS.



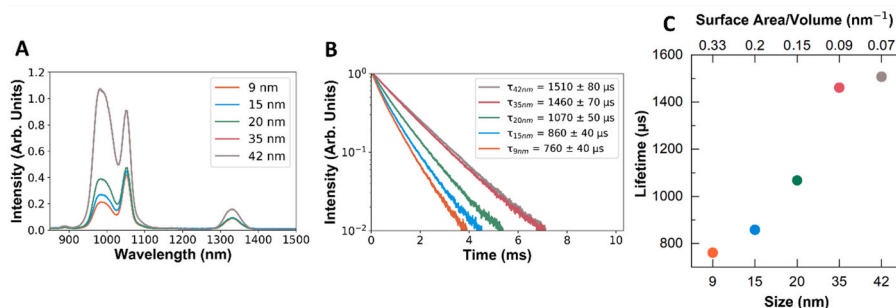


**Fig. 2.** Spectroscopic characterization. (A) infrared emission spectrum of five different sizes of  $\tau$ NPs modified with PAA, dispersed in PBS and excited at 808 nm. (B) Normalized fluorescence decay curves of the emission observed at 980 nm corresponding to the five different sizes of  $\tau$ NPs modified with PAA in PBS and excited at 808 nm. (C) Fluorescence lifetime depending on the size and surface-to-volume ratio of five different sizes of  $\tau$ NPs.

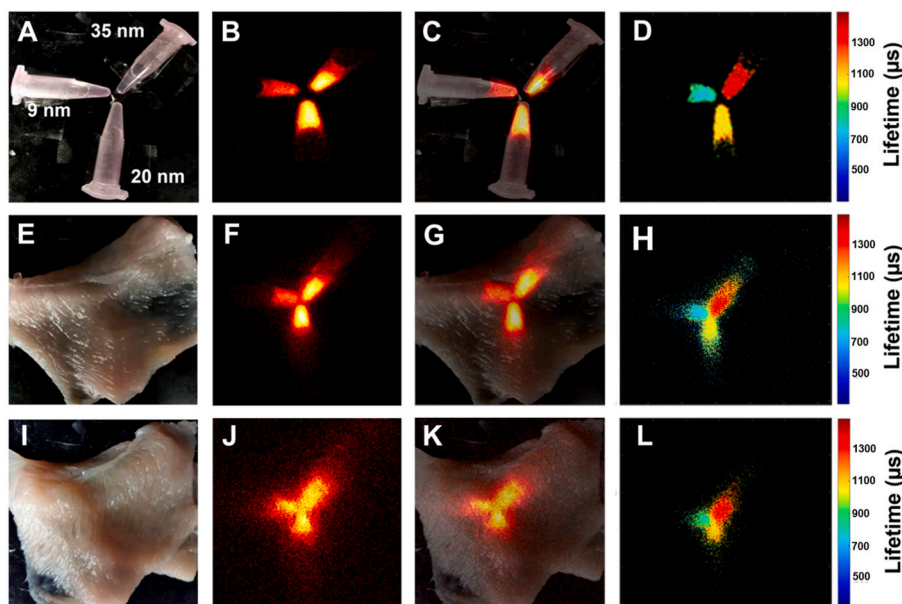


**Fig. 3.** Lifetime mapping with  $\tau$ NPs. (A) Optical image, (B) infrared image, (C) merged image of the optical image and infrared image and (D) fluorescence lifetime mapping image of different  $\tau$ NP dispersions in PBS, specifically with 9, 20 and 35 nm core diameters (5 mg/mL, 5 mg/mL and 1 mg/mL respectively). (E) Optical image, (F) infrared image, (G) merged image of optical image and infrared image and (H) fluorescence lifetime mapping image of the same  $\tau$ NPs covered with 2 mm chicken. (I) Optical image, (J) infrared image, (K) merged image between optical image and infrared image and (L) fluorescence lifetime mapping image of the same  $\tau$ NP dispersions covered with 5 mm chicken.

lifetimes. This is a relevant point with important practical implications. When acquiring lifetime-based *in vivo* imaging the signal level plays a pivotal role as it determines the accuracy and reliability of the lifetime determination. Being able to provide luminescent probes with similar emitted intensities but different lifetimes ensures a similar degree of accuracy for lifetime determination of the different probes [67]. Moreover, the different contrast agents still provide similar emitted intensities in the presence of tissues. This indicates that the emission of the three samples is equally influenced by the tissue extinction, as expected since the three samples here analysed show the same emission spectra and thus are affected by the same extinction coefficients. Furthermore, Fig. S7 confirms that the lifetimes of our samples can be determined independently of the tissues in which they are injected. This constitutes a clear advantage over probes designed for spectral multiplexed imaging that are affected by different tissue extinction coefficients in their spectral regions.

Furthermore, to demonstrate the applicability of our nanoparticles in a biomedical context, we first performed an *in vitro* cell viability assay before moving to a mouse model. The  $\tau$ NPs were incubated for 6 and 24 h with human HeLa (Fig. 4A) and HaCaT (human epithelial cervical cancer and immortalized keratinocytes, respectively) cell lines (Fig. 4B) at two different concentrations. No viability problems were observed as expected for RENPs with a biocompatible coating (see the Supplementary Data for experimental details). This allowed us to design a simple

experiment employing two types of  $\tau$ NPs with a difference in their measured lifetime for a subcutaneous injection in each flank of the animal. Fig. 4C shows the image obtained by the infrared camera, demonstrating similar NIR-II intensities for both injection sites and no differentiation of the  $\tau$ NPs is possible. Fig. 4D and merged Fig. 4E, on the other hand, present the lifetime map obtained after processing the series of time-gated images, demonstrating a sub-tissue lifetime of around 0.9 ms on the left and 1.4 ms on the right flank of the animal. The result illustrated in here clearly showcases the capacity of the time-gated technique in combination with the different  $\tau$ NPs to achieve multiplexing *in vivo*, highlighting the usefulness of working in the time domain.

#### 4. Conclusions

In summary, we developed a series of nanoparticles with the same chemical composition and hydrodynamic diameter but different crystal size. This was achieved through a careful selection of the reaction parameters and control of the host material, dopants and a layer-by-layer technique to grow the inorganic crystal, followed by the bio-functionalisation of the surface. As a result,  $\tau$ NPs with different lifetimes but otherwise similar behaviour for their use as multiplexing-capable contrast agent were obtained and carefully characterized. Small changes in crystal size resulted in relevant lifetime changes, making

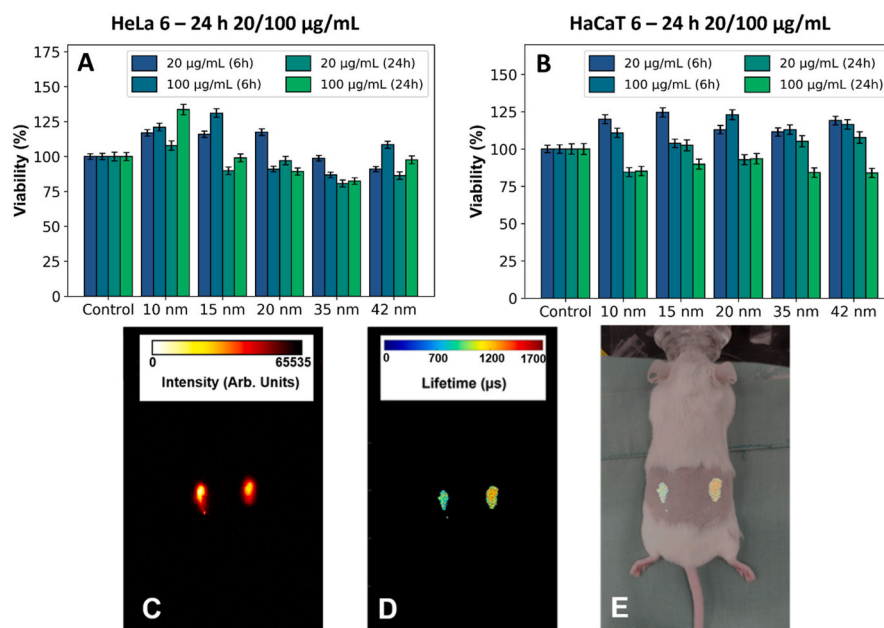


**Fig. 4.** Cell viability, *in vivo* imaging and lifetime mapping. (A) Cell viability performed on HeLa cells and (B) HaCaT cells after 6 and 24 h of cell incubation with five different sizes of  $\tau$ NPs at a concentration of 20 and 100  $\mu\text{g/mL}$ . (C) Infrared image, (D) merge between optical image and infrared image and (E) fluorescence lifetime mapping image after 50  $\mu\text{L}$  injection of  $\tau$ NP (20 nm and 35 nm) dispersions in PBS (5 mg/mL and 1 mg/mL, respectively).

multiplexed time-gated NIR imaging possible. This was proven by *ex vivo* experiments with biological tissues, allowing the transformation of the time-gated images into tissue-independent lifetime maps. Finally, a simple *in vivo* proof-of-concept model with two subcutaneous injections also demonstrated their applicability as NIR multiplexing contrast agents for *in vivo* experiments, highlighting how a strategy as simple as controlling the crystal size can yield rare-earth-based nanoparticles useable as contrast agents for *in vivo* multiplexing.

#### CRediT authorship contribution statement

**Jingke Yao:** Investigation, Data curation. **Gabriel López-Peña:** Investigation, Data curation, Visualization. **José Lifante:** Investigation. **M. Carmen Iglesias-de la Cruz:** Investigation, Data curation, Resources. **Riccardo Marin:** Supervision, Visualization, Writing – original draft, Writing. **Emma Martín Rodríguez:** Data curation, Methodology, Formal analysis, Software, Writing – original draft, Writing. **Daniel Jaque:** Conceptualization, Methodology, Funding acquisition. **Dirk H. Ortgies:** Supervision, Methodology, Resources, Writing – original draft, Writing.

#### Declaration of competing interest

The authors declare that they have no known competing financial interests or personal relationships that could have appeared to influence the work reported in this paper.

#### Data availability

Data will be made available on request.

#### Acknowledgements

J.Y. and G.L.P. contributed equally. The authors are grateful to Dr. Francisco Sanz from Universidad Autónoma de Madrid for the generous gift of the cells. This work was financed by the Spanish Ministerio de Ciencia e Innovación under projects PID2019-106211RB-I00 and PID2020-118878RB-I00, by the Instituto de Salud Carlos III (PI19/

00565), by the Comunidad Autónoma de Madrid (CAM) S2017/BMD3867 RENIM-CM grant and co-financed by the European structural and investment fund. Additional funding was provided by the European Union Horizon 2020 FETOpen project NanoTBTech (801305), the CAM young investigator project SI3/PJI/2021-00211 the Fundación para la Investigación Biomédica del Hospital Universitario Ramón y Cajal project IMP21\_A4 (2021/0427), and also by COST action CA17140. R. M. acknowledges the support of the European Union's Horizon 2020 research and innovation program under the Marie Skłodowska-Curie Grant Agreement No. 797945 (LANTERNS). J.Y. acknowledges the support from the China Scholarship Council (CSC File No.201704910867).

#### Appendix A. Supplementary data

Supplementary data to this article can be found online at <https://doi.org/10.1016/j.omx.2022.100225>.

#### References

- [1] D. Jaque, C. Richard, B. Viana, K. Soga, X. Liu, J. García Solé, Inorganic nanoparticles for optical bioimaging, *Adv. Opt. Photon* 8 (2016) 1, <https://doi.org/10.1364/AOP.8.000001>.
- [2] Kenry, Y. Duan, B. Liu, Recent advances of optical imaging in the second near-infrared window, *Adv. Mater.* 30 (2018) 1–19, <https://doi.org/10.1002/adma.201802394>.
- [3] A.V. Dsouza, H. Lin, E.R. Henderson, K.S. Samkoe, B.W. Pogue, Review of fluorescence guided surgery systems: identification of key performance capabilities beyond indocyanine green imaging, *J. Biomed. Opt.* 21 (2016), 080901, <https://doi.org/10.1117/1.JBO.21.8.080901>.
- [4] A. Benayas, Near Infrared-Emitting Nanoparticles for Biomedical Applications, Springer International Publishing, Cham, 2020, <https://doi.org/10.1007/978-3-030-32036-2>.
- [5] G. Hong, A.L. Antaris, H. Dai, Near-infrared fluorophores for biomedical imaging, *Nat. Biomed. Eng.* 1 (2017), 0010, <https://doi.org/10.1038/s41551-016-0010>.
- [6] E. Hemmer, N. Venkatachalam, H. Hyodo, A. Hattori, Y. Ebina, H. Kishimoto, K. Soga, Upconverting and NIR emitting rare earth based nanostructures for NIR-bioimaging, *Nanoscale* 5 (2013) 11339–11361, <https://doi.org/10.1039/c3nr02286b>.
- [7] R. Weissleder, A clearer vision for in vivo imaging, *Nat. Biotechnol.* 19 (2001) 316–317, <https://doi.org/10.1038/86684>.
- [8] A.M. Smith, M.C. Mancini, S. Nie, Second window for in vivo imaging, *Nat. Nanotechnol.* 4 (2009) 710–711, <https://doi.org/10.1038/nnano.2009.326>.

- [9] E. Ximendes, A. Benayas, D. Jaque, R. Marin, Quo vadis, nanoparticle-enabled in vivo fluorescence imaging? *ACS Nano* 15 (2021) 1917–1941, <https://doi.org/10.1021/acsnano.0c08349>.
- [10] Z. Hu, C. Fang, B. Li, Z. Zhang, C. Cao, M. Cai, S. Su, X. Sun, X. Shi, C. Li, T. Zhou, Y. Zhang, C. Chi, P. He, X. Xia, Y. Chen, S.S. Gambhir, Z. Cheng, J. Tian, First-in-human liver-tumour surgery guided by multispectral fluorescence imaging in the visible and near-infrared-I/II windows, *Nat. Biomed. Eng.* 4 (2020) 259–271, <https://doi.org/10.1038/s41551-019-0494-0>.
- [11] C. Li, G. Chen, Y. Zhang, F. Wu, Q. Wang, Advanced fluorescence imaging technology in the near-infrared-II window for biomedical applications, *J. Am. Chem. Soc.* 142 (2020) 14789–14804, <https://doi.org/10.1021/jacs.0c07022>.
- [12] K. Welscher, S.P. Sherlock, H. Dai, Deep-tissue anatomical imaging of mice using carbon nanotube fluorophores in the second near-infrared window, *Proc. Natl. Acad. Sci. USA* 108 (2011) 8943–8948, <https://doi.org/10.1073/pnas.1014501108>.
- [13] J.T. Robinson, G. Hong, Y. Liang, B. Zhang, O.K. Yaghi, H. Dai, In vivo fluorescence imaging in the second near-infrared window with long circulating carbon nanotubes capable of ultrahigh tumor uptake, *J. Am. Chem. Soc.* 134 (2012) 10664–10669, <https://doi.org/10.1021/ja303737a>.
- [14] R. Bhavane, Z. Starosolski, I. Stupin, K.B. Ghaghada, A. Annapragada, NIR-II fluorescence imaging using indocyanine green nanoparticles, *Sci. Rep.* 8 (2018), 14455, <https://doi.org/10.1038/s41598-018-32754-y>.
- [15] T.V. De Medeiros, J. Manioudakis, F. Noun, J.R. Macairan, F. Victoria, R. Naccache, Microwave-assisted synthesis of carbon dots and their applications, *J. Mater. Chem. C* 7 (2019) 7175–7195, <https://doi.org/10.1039/c9tc01640f>.
- [16] J. Huang, C. Xie, X. Zhang, Y. Jiang, J. Li, Q. Fan, K. Pu, Renal-clearable molecular semiconductor for second near-infrared fluorescence imaging of kidney dysfunction, *Angew. Chem. Int. Ed.* 58 (2019) 15120–15127, <https://doi.org/10.1002/anie.201909560>.
- [17] Y. Lyu, J. Li, K. Pu, Second near-infrared absorbing agents for photoacoustic imaging and photothermal therapy, *Small Methods* 3 (2019), 1900553, <https://doi.org/10.1002/smt.201900553>.
- [18] Y. Jiang, P.K. Upputuri, C. Xie, Z. Zeng, A. Sharma, X. Zhen, J. Li, J. Huang, M. Pramanik, K. Pu, Metabolizable semiconducting polymer nanoparticles for second near-infrared photoacoustic imaging, *Adv. Mater.* 31 (2019), 1808166, <https://doi.org/10.1002/adma.201808166>.
- [19] Q. Miao, K. Pu, Organic semiconducting agents for deep-tissue molecular imaging: second near-infrared fluorescence, self-luminescence, and photoacoustics, *Adv. Mater.* 30 (2018), 1801778, <https://doi.org/10.1002/adma.201801778>.
- [20] A. Benayas, F. Ren, E. Carrasco, V. Marzal, B. del Rosal, B.A. Gonfa, Á. Juarraz, F. Sanz-Rodríguez, D. Jaque, J. García-Solé, D. Ma, F. Vetrone, PbS/CdS/ZnS quantum dots: a multifunctional platform for in vivo near-infrared low-dose fluorescence imaging, *Adv. Funct. Mater.* 25 (2015) 6650–6659, <https://doi.org/10.1002/adfm.201502632>.
- [21] Y. Imamura, S. Yamada, S. Tsuboi, Y. Nakane, Y. Tsukasaki, A. Komatsuzaki, T. Jin, Near-infrared emitting PbS quantum dots for in vivo fluorescence imaging of the thrombotic state in septic mouse brain, *Molecules* 21 (2016), <https://doi.org/10.3390/molecules21081080>.
- [22] S. Jeong, Y. Jung, S. Bok, Y.-M. Ryu, S. Lee, Y.-E. Kim, J. Song, M. Kim, S.-Y. Kim, G.-O. Ahn, S. Kim, Multiplexed in vivo imaging using size-controlled quantum dots in the second near-infrared window, *Adv. Healthc. Mater.* 7 (2018), 1800695, <https://doi.org/10.1002/adhm.201800695>.
- [23] S.I. Sadovnikov, A.I. Gusev, Recent progress in nanostructured silver sulfide: from synthesis and nonstoichiometry to properties, *J. Mater. Chem. A* 5 (2017) 17676–17704, <https://doi.org/10.1039/c7ta04949h>.
- [24] Y. Zhang, G. Hong, Y. Zhang, G. Chen, F. Li, H. Dai, Q. Wang, Ag 2 S quantum dot: a bright and biocompatible fluorescent nanoprobe in the second near-infrared window, *ACS Nano* 6 (2012) 3695–3702, <https://doi.org/10.1021/nn301218z>.
- [25] G. Hong, J.T. Robinson, Y. Zhang, S. Diao, A.L. Antaris, Q. Wang, H. Dai, In vivo fluorescence imaging with Ag 2 S quantum dots in the second near-infrared region, *Angew. Chem. Int. Ed.* 51 (2012) 9818–9821, <https://doi.org/10.1002/anie.201206059>.
- [26] X.D. Zhang, H. Wang, A.L. Antaris, L. Li, S. Diao, R. Ma, A. Nguyen, G. Hong, Z. Ma, J. Wang, S. Zhu, J.M. Castellano, T. Wyss-Coray, Y. Liang, J. Luo, H. Dai, Traumatic brain injury imaging in the second near-infrared window with a molecular fluorophore, *Adv. Mater.* 28 (2016) 6872–6879, <https://doi.org/10.1002/adma.201600706>.
- [27] A.L. Antaris, H. Chen, K. Cheng, Y. Sun, G. Hong, C. Qu, S. Diao, Z. Deng, X. Hu, B. Zhang, X. Zhang, O.K. Yaghi, Z.R. Alamparabail, X. Hong, Z. Cheng, H. Dai, A small-molecule dye for NIR-II imaging, *Nat. Mater.* 15 (2016) 235–242, <https://doi.org/10.1038/nmat4476>.
- [28] Q. Yang, Z. Ma, H. Wang, B. Zhou, S. Zhu, Y. Zhong, J. Wang, H. Wan, A. Antaris, R. Ma, X. Zhang, J. Yang, X. Zhang, H. Sun, W. Liu, Y. Liang, H. Dai, Rational design of molecular fluorophores for biological imaging in the NIR-II window, *Adv. Mater.* 29 (2017), <https://doi.org/10.1002/adma.201605497>.
- [29] E.D. Cosco, J.R. Caram, O.T. Bruns, D. Franke, R.A. Day, E.P. Farr, M.G. Bawendi, E.M. Sletten, Flavylium polymethine fluorophores for near- and shortwave infrared imaging, *Angew. Chem. Int. Ed.* 56 (2017) 13126–13129, <https://doi.org/10.1002/anie.201706974>.
- [30] E.D. Cosco, B.A. Arús, A.L. Spearman, T.L. Atallah, I. Lim, O.S. Leland, J.R. Caram, T.S. Bischof, O.T. Bruns, E.M. Sletten, Bright chromenyl polymethine dyes enable fast, four-color in vivo imaging with shortwave infrared detection, *J. Am. Chem. Soc.* 143 (2021) 6836–6846, <https://doi.org/10.1021/jacs.0c11599>.
- [31] L. Labrador-Páez, E.C. Ximendes, P. Rodríguez-Sevilla, D.H. Ortigies, U. Rocha, C. Jacinto, E. Martín Rodríguez, P. Haro-González, D. Jaque, Core-shell rare-earth-doped nanostructures in biomedicine, *Nanoscale* 10 (2018) 12935–12956, <https://doi.org/10.1039/C8NR02307G>.
- [32] Y. Liu, D. Tu, H. Zhu, X. Chen, Lanthanide-doped luminescent nanoprobes: controlled synthesis, optical spectroscopy, and bioapplications, *Chem. Soc. Rev.* 42 (2013) 6924, <https://doi.org/10.1039/c3cs60060b>.
- [33] B. Liu, C. Li, P. Yang, Z. Hou, J. Lin, 808-nm-Light-Excited lanthanide-doped nanoparticles: rational design, luminescence control and theranostic applications, *Adv. Mater.* 29 (2017), 1605434, <https://doi.org/10.1002/adma.201605434>.
- [34] I. Villa, A. Vedda, I.X. Cantarelli, M. Pedroni, F. Piccinelli, M. Bettinelli, A. Speghini, M. Quintanilla, F. Vetrone, U. Rocha, C. Jacinto, E. Carrasco, F. Sanz-Rodríguez, Á. Juarraz, B. del Rosal, D.H. Ortigies, P. Haro Gonzalez, J. García Solé, D. Jaque García, 1.3  $\mu\text{m}$  emitting SrF<sub>2</sub>:Nd<sup>3+</sup> nanoparticles for high contrast in vivo imaging in the second biological window, *Nano Res.* 8 (2015) 649–665, <https://doi.org/10.1007/s12274-014-0549-1>.
- [35] B. del Rosal, I. Villa, D. Jaque, F. Sanz-Rodríguez, In vivo autofluorescence in the biological windows: the role of pigmentation, *J. Biophot.* 9 (2016) 1059–1067, <https://doi.org/10.1002/jbio.201500271>.
- [36] I. Villa, A. Vedda, I.X. Cantarelli, M. Pedroni, F. Piccinelli, M. Bettinelli, A. Speghini, M. Quintanilla, F. Vetrone, U. Rocha, C. Jacinto, E. Carrasco, F. Sanz-Rodríguez, Á. Juarraz, B. del Rosal, D.H. Ortigies, P. Haro Gonzalez, J. García Solé, D. Jaque García, 1.3  $\mu\text{m}$  emitting SrF<sub>2</sub>:Nd<sup>3+</sup> nanoparticles for high contrast in vivo imaging in the second biological window, *Nano Res.* 8 (2015) 649–665, <https://doi.org/10.1007/s12274-014-0549-1>.
- [37] J. Lifante, Y. Shen, E. Ximendes, E. Martín Rodríguez, D.H. Ortigies, The role of tissue fluorescence in in vivo optical biotomography, *J. Appl. Phys.* 128 (2020), 171101, <https://doi.org/10.1063/5.0021854>.
- [38] B. del Rosal, A. Benayas, Strategies to overcome autofluorescence in nanoprobes-driven in vivo fluorescence imaging, *Small Methods* 2 (2018), 1800075, <https://doi.org/10.1002/smt.201800075>.
- [39] D.H. Ortigies, E. Martín Rodríguez, Near infrared-emitting bioprobes for low-autofluorescence imaging techniques, in: *Near Infrared-Emitting Nanoparticles Biomed. Appl.*, Springer International Publishing, Cham, 2020, pp. 199–229, [https://doi.org/10.1007/978-3-030-32036-2\\_9](https://doi.org/10.1007/978-3-030-32036-2_9).
- [40] B. del Rosal, D.H. Ortigies, N. Fernández, F. Sanz-Rodríguez, D. Jaque, E. Martín Rodríguez, Overcoming autofluorescence: long-lifetime infrared nanoparticles for time-gated in vivo imaging, *Adv. Mater.* 28 (2016) 10188–10193, <https://doi.org/10.1002/adma.201603583>.
- [41] M. Tan, B. del Rosal, Y. Zhang, E. Martín Rodríguez, J. Hu, Z. Zhou, R. Fan, D. H. Ortigies, N. Fernández, I. Chaves-Coira, Á. Núñez, D. Jaque, G. Chen, Rare-earth-doped fluoride nanoparticles with engineered long luminescence lifetime for time-gated in vivo optical imaging in the second biological window, *Nanoscale* 10 (2018) 17771–17780, <https://doi.org/10.1039/C8NR02382D>.
- [42] Y. Gu, Z. Guo, W. Yuan, M. Kong, Y. Liu, Y. Gao, W. Feng, F. Wang, J. Zhou, D. Jin, F. Li, High-sensitivity imaging of time-domain near-infrared light transducer, *Nat. Photonics* 13 (2019) 525–531, <https://doi.org/10.1038/s41566-019-0437-z>.
- [43] M.Y. Berezin, S. Achilefu, Fluorescence lifetime measurements and biological imaging, *Chem. Rev.* 110 (2010) 2641–2684, <https://doi.org/10.1021/cr900343z>.
- [44] J.-H. Park, L. Gu, G. von Maltzahn, E. Ruoslahti, S.N. Bhatia, M.J. Sailor, Biodegradable luminescent porous silicon nanoparticles for in vivo applications, *Nat. Mater.* 8 (2009) 331–336, <https://doi.org/10.1038/nmat2398>.
- [45] K.Y. Zhang, Q. Yu, H. Wei, S. Liu, Q. Zhao, W. Huang, Long-lived emissive probes for time-resolved photoluminescence bioimaging and biosensing, *Chem. Rev.* 118 (2018) 1770–1839, <https://doi.org/10.1021/acs.chemrev.7b00425>.
- [46] L. Gu, D.J. Hall, Z. Qin, E. Anglin, J. Joo, D.J. Mooney, S.B. Howell, M.J. Sailor, In vivo time-gated fluorescence imaging with biodegradable luminescent porous silicon nanoparticles, *Nat. Commun.* 4 (2013) 2326, <https://doi.org/10.1038/ncomms3326>.
- [47] W. Yang, S.-L. Chen, Time-gated fluorescence imaging: advances in technology and biological applications, *J. Innov. Opt. Health Sci.* 13 (2020), 2030006, <https://doi.org/10.1142/S1793545820300062>.
- [48] D. Jin, Y. Lu, R.C. Leif, S. Yang, M. Rajendran, L.W. Miller, How to build a time-gated luminescence microscope, *Curr. Protoc. Cytom.* 67 (2014), <https://doi.org/10.1002/0471142956.cy0222s67>, 2.22.1–2.22.36.
- [49] X. Zheng, X. Zhu, Y. Lu, J. Zhao, W. Feng, G. Jia, F. Wang, F. Li, D. Jin, High-contrast visualization of upconversion luminescence in mice using time-gating approach, *Anal. Chem.* 88 (2016) 3449–3454, <https://doi.org/10.1021/acs.analchem.5b04626>.
- [50] B. del Rosal, D.H. Ortigies, N. Fernández, F. Sanz-Rodríguez, D. Jaque, E. Martín Rodríguez, Overcoming autofluorescence: long-lifetime infrared nanoparticles for time-gated in vivo imaging, *Adv. Mater.* 28 (2016) 10188–10193, <https://doi.org/10.1002/adma.201603583>.
- [51] L. Cai, Y. Huang, P. Sun, W. Zheng, S. Zhou, P. Huang, J. Wei, D. Tu, X. Chen, Z. Liang, Accurate detection of  $\beta$ -hCG in women's serum and cervical secretions for predicting early pregnancy viability based on time-resolved luminescent lanthanide nanoprobes, *Nanoscale* 12 (2020) 6729–6735, <https://doi.org/10.1039/C9NR10973K>.
- [52] Y. Lu, J. Lu, J. Zhao, J. Cusido, F.M. Raymo, J. Yuan, S. Yang, R.C. Leif, Y. Huo, J. A. Piper, J. Paul Robinson, E.M. Goldys, D. Jin, On-the-fly decoding luminescence lifetimes in the microsecond region for lanthanide-encoded suspension arrays, *Nat. Commun.* 5 (2014), <https://doi.org/10.1038/ncomms4741>.
- [53] D. Jin, J.A. Piper, Time-gated luminescence microscopy allowing direct visual inspection of lanthanide-stained microorganisms in background-free condition, *Anal. Chem.* 83 (2011) 2294–2300, <https://doi.org/10.1021/ac103207r>.



- [54] W.C. Chan, D.J. Maxwell, X. Gao, R.E. Bailey, M. Han, S. Nie, Luminescent quantum dots for multiplexed biological detection and imaging, *Curr. Opin. Biotechnol.* 13 (2002) 40–46, [https://doi.org/10.1016/S0958-1669\(02\)00282-3](https://doi.org/10.1016/S0958-1669(02)00282-3).
- [55] J.R. Mansfield, K.W. Gossage, C.C. Hoyt, R.M. Levenson, Autofluorescence removal, multiplexing, and automated analysis methods for in-vivo fluorescence imaging, *J. Biomed. Opt.* 10 (2005), 041207, <https://doi.org/10.1117/1.2032458>.
- [56] Y. Li, Y.T.H. Cu, D. Luo, Multiplexed detection of pathogen DNA with DNA-based fluorescence nanobarcodes, *Nat. Biotechnol.* 23 (2005) 885–889, <https://doi.org/10.1038/nbt1106>.
- [57] K. Heinzmann, L.M. Carter, J.S. Lewis, E.O. Aboagye, Multiplexed imaging for diagnosis and therapy, *Nat. Biomed. Eng.* 1 (2017) 697–713, <https://doi.org/10.1038/s41551-017-0131-8>.
- [58] A.Z. Abbasi, F. Amin, T. Niebling, S. Friede, M. Ochs, S. Carregal-Romero, J.-M. Montenegro, P. Rivera Gil, W. Heimbrot, W.J. Parak, How colloidal nanoparticles could facilitate multiplexed measurements of different analytes with analyte-sensitive organic fluorophores, *ACS Nano* 5 (2011) 21–25, <https://doi.org/10.1021/nn1034026>.
- [59] K. Hoffmann, T. Behnke, D. Drescher, J. Kneipp, U. Resch-Genger, Near-infrared-Emitting nanoparticles for lifetime-based multiplexed analysis and imaging of living cells, *ACS Nano* 7 (2013) 6674–6684, <https://doi.org/10.1021/nn4029458>.
- [60] A. Yakovlev, R. Ziniuk, D. Wang, B. Xue, L.O. Vretik, O.A. Nikolaeva, M. Tan, G. Chen, Y.L. Slominskii, J. Qu, T.Y. Ohulchanskyy, Hyperspectral multiplexed biological imaging of nanoprobe emitting in the short-wave infrared region, *Nanoscale Res. Lett.* 14 (2019) 243, <https://doi.org/10.1186/s11671-019-3068-x>.
- [61] R. Tian, H. Ma, S. Zhu, J. Lau, R. Ma, Y. Liu, L. Lin, S. Chandra, S. Wang, X. Zhu, H. Deng, G. Niu, M. Zhang, A.L. Antaris, K.S. Hettie, B. Yang, Y. Liang, X. Chen, Multiplexed NIR-II probes for lymph node-invaded cancer detection and imaging-guided surgery, *Adv. Mater.* 32 (2020) 1–10, <https://doi.org/10.1002/adma.201907365>.
- [62] Y. Lu, J. Zhao, R. Zhang, Y. Liu, D. Liu, E.M. Goldys, X. Yang, P. Xi, A. Sunna, J. Lu, Y. Shi, R.C. Leif, Y. Huo, J. Shen, J.A. Piper, J.P. Robinson, D. Jin, Tunable lifetime multiplexing using luminescent nanocrystals, *Nat. Photonics* 8 (2014) 32–36, <https://doi.org/10.1038/nphoton.2013.322>.
- [63] Y. Fan, P. Wang, Y. Lu, R. Wang, L. Zhou, X. Zheng, X. Li, J.A. Piper, F. Zhang, Lifetime-engineered NIR-II nanoparticles unlock multiplexed in vivo imaging, *Nat. Nanotechnol.* 13 (2018) 941–946, <https://doi.org/10.1038/s41565-018-0221-0>.
- [64] H. Li, M. Tan, X. Wang, F. Li, Y. Zhang, L. Zhao, C. Yang, G. Chen, Temporal multiplexed in vivo upconversion imaging, *J. Am. Chem. Soc.* 142 (2020) 2023–2030, <https://doi.org/10.1021/jacs.9b11641>.
- [65] S. Cheng, Q. Liu, X. Zhou, Y. Gu, W. Yuan, W. Feng, F. Li, Reversible ratiometric probe combined with the time-gated method for accurate in vivo gastrointestinal pH sensing, *ACS Appl. Mater. Interfaces* 12 (2020) 25557–25564, <https://doi.org/10.1021/acsami.0c04237>.
- [66] M. Kong, Y. Gu, Y. Liu, Y. Shi, N. Wu, W. Feng, F. Li, Luminescence lifetime-based in vivo detection with responsive rare earth-dye nanocomposite, *Small* 15 (2019), 1904487, <https://doi.org/10.1002/sml.201904487>.
- [67] F. Zhang, X. Zhu, X. Liu, M. Zhao, P. Pei, Y. Chen, Y. Yang, L. Lu, P. Yu, C. Sun, J. Ming, I. Abraham, H. Zhang, A.M. El-Toni, A. Khan, High-fidelity NIR-II multiplexed lifetime bioimaging with bright double interfaced lanthanide nanoparticles, *Angew. Chem.* (2021), <https://doi.org/10.1002/ange.202108124>.
- [68] X. Zhang, Z. Zhao, X. Zhang, D.B. Cordes, B. Weeks, B. Qiu, K. Madanan, D. Sardar, J. Chaudhuri, Magnetic and optical properties of NaGdF<sub>4</sub>:Nd<sup>3+</sup>, Yb<sup>3+</sup>, Tm<sup>3+</sup> nanocrystals with upconversion/downconversion luminescence from visible to the near-infrared second window, *Nano Res.* 8 (2015) 636–648, <https://doi.org/10.1007/s12274-014-0548-2>.
- [69] L. Balogh, S.S. Nigavekar, B.M. Nair, W. Lesniak, C. Zhang, L.Y. Sung, M.S. T. Kariapper, A. El-Jawahri, M. Llanes, B. Bolton, F. Mamou, W. Tan, A. Hutson, L. Minc, M.K. Khan, Significant effect of size on the in vivo biodistribution of gold composite nanodevices in mouse tumor models, *Nanomed. Nanotechnol. Biol. Med.* 3 (2007) 281–296, <https://doi.org/10.1016/j.nano.2007.09.001>.
- [70] F. Alexis, E. Pridgen, L.K. Molnar, O.C. Farokhzad, Factors affecting the clearance and biodistribution of polymeric nanoparticles, *Mol. Pharm.* 5 (2008) 505–515, <https://doi.org/10.1021/mp800051m>.
- [71] L. Li, G. Tian, Y. Deng, Y. Wang, Z. Cao, F. Ling, Y. Li, S. Jiang, G. Xiang, X. Zhou, Constructing ultra-sensitive dual-mode optical thermometers: utilizing FIR of Mn<sup>4+</sup>/Eu<sup>3+</sup> and lifetime of Mn<sup>4+</sup> based on double perovskite tellurite phosphor, *Opt Express* 28 (2020), 33747, <https://doi.org/10.1364/OE.409242>.
- [72] P. Du, X. Wan, L. Luo, W. Li, L. Li, Thermally stable Tb<sup>3+</sup>/Eu<sup>3+</sup>-codoped K<sub>0.3</sub>Bi<sub>0.7</sub>F<sub>2.4</sub> nanoparticles with multicolor luminescence for white-light-emitting diodes, *ACS Appl. Nano Mater.* 4 (2021) 7062–7071, <https://doi.org/10.1021/acsnano.1c01072>.
- [73] X. Li, D. Shen, J. Yang, C. Yao, R. Che, F. Zhang, D. Zhao, Successive layer-by-layer strategy for multi-shell epitaxial growth: shell thickness and doping position dependence in upconverting optical properties, *Chem. Mater.* 25 (2013) 106–112, <https://doi.org/10.1021/cm3033498>.
- [74] M. Xu, J. Zhu, F. Wang, Y. Xiong, Y. Wu, Q. Wang, J. Weng, Z. Zhang, W. Chen, S. Liu, Improved in vitro and in vivo biocompatibility of graphene oxide through surface modification: poly(acrylic acid)-functionalization is superior to PEGylation, *ACS Nano* 10 (2016) 3267–3281, <https://doi.org/10.1021/acsnano.6b00539>.
- [75] X. Miao, W. Xu, H. Cha, Y. Chang, I.T. Oh, K.S. Chae, T. Tegaaw, S.L. Ho, S.J. Kim, G.H. Lee, Ultrasmall Gd<sub>2</sub>O<sub>3</sub> nanoparticles surface-coated by polyacrylic acid (PAA) and their PAA-size dependent relaxometric properties, *Appl. Surf. Sci.* 477 (2019) 111–115, <https://doi.org/10.1016/j.apsusc.2017.11.225>.
- [76] J.W. Stouwdam, F.C.J.M. Van Veggel, Near-infrared emission of redispersible Er<sup>3+</sup>, Nd<sup>3+</sup>, and Ho<sup>3+</sup> doped LaF<sub>3</sub> nanoparticles, *Nano Lett.* 2 (2002) 733–737, <https://doi.org/10.1021/nl025562q>.
- [77] J. Zhao, Z. Lu, Y. Yin, C. McRae, J.A. Piper, J.M. Dawes, D. Jin, E.M. Goldys, Upconversion luminescence with tunable lifetime in NaYF<sub>4</sub>:Yb,Er nanocrystals: role of nanocrystal size, *Nanoscale* 5 (2013) 944–952, <https://doi.org/10.1039/c2nr32482b>.
- [78] S. Mei, J. Zhou, H.T. Sun, Y. Cai, L.D. Sun, D. Jin, C.H. Yan, Networking state of ytterbium ions probing the origin of luminescence quenching and activation in nanocrystals, *Adv. Sci.* 8 (2021) 1–9, <https://doi.org/10.1002/advs.202003325>.
- [79] M. Quintanilla, E. Hemmer, J. Marques-Hueso, S. Rohani, G. Lucchini, M. Wang, R. Zamani, V. Roddatis, A. Speghini, B.S. Richards, F. Vetrone, Cubic: versus hexagonal-phase, size and morphology effects on the photoluminescence quantum yield of NaGdF<sub>4</sub>:Er<sup>3+</sup>/Yb<sup>3+</sup>-upconverting nanoparticles, *Nanoscale* 14 (2022) 1492–1504, <https://doi.org/10.1039/d1nr06319g>.